

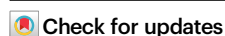


Temperature-dependent rearrangement of gas molecules in ultramicroporous materials for tunable adsorption of CO₂ and C₂H₂

Received: 14 February 2023

Accepted: 5 June 2023

Published online: 24 June 2023



Zhaoqiang Zhang^{1,8}, Yinlin Chen^{2,8}, Kungang Chai³, Chengjun Kang¹, Shing Bo Peh¹, He Li¹, Junyu Ren¹, Xiansong Shi¹, Xue Han⁴, Catherine Dejoie⁵, Sarah J. Day⁶, Sihai Yang^{2,7}✉ & Dan Zhao¹✉

The interactions between adsorbed gas molecules within porous metal-organic frameworks are crucial to gas selectivity but remain poorly explored. Here, we report the modulation of packing geometries of CO₂ and C₂H₂ clusters within the ultramicroporous CUK-1 material as a function of temperature. In-situ synchrotron X-ray diffraction reveals a unique temperature-dependent reversal of CO₂ and C₂H₂ adsorption affinities on CUK-1, which is validated by gas sorption and dynamic breakthrough experiments, affording high-purity C₂H₂ (99.95%) from the equimolar mixture of C₂H₂/CO₂ via a one-step purification process. At low temperatures (<253 K), CUK-1 preferentially adsorbs CO₂ with both high selectivity (>10) and capacity (170 cm³ g⁻¹) owing to the formation of CO₂ tetramers that simultaneously maximize the guest-guest and host-guest interactions. At room temperature, conventionally selective adsorption of C₂H₂ is observed. The selectivity reversal, structural robustness, and facile regeneration of CUK-1 suggest its potential for producing high-purity C₂H₂ by temperature-swing sorption.

Host-guest chemistry is fundamental to the selectivity of many molecular recognition systems^{1–5}. The optimization of cooperative interactions, such as electrostatic interactions and hydrogen bonding, plays a crucial role in the design of efficient molecular recognition systems, particularly in porous materials. These cooperative interactions are essential for achieving high performance in gas adsorption, sensing, and catalysis applications^{1,3,6–17}. On the other hand, guest-guest interactions or the formation of guest clusters also play an important role in molecular recognition. However, the direct observation and control of guest-guest interactions within confined nanovoids of porous materials is highly challenging and remains poorly explored^{18–20}. Screening new host-guest and guest-guest

interactions can promote the design of new functional porous materials^{1,21}.

Ultramicroporous metal-organic frameworks (MOFs), featuring highly inerratic porosity, tunable pore chemistry, and designable structures, provide a unique platform to explore host-guest interactions^{11,22–27}. In particular, the modular nature and reticular structure endow ultramicroporous MOFs with the possibility to precisely control the host-guest and guest-guest interactions within the pores^{28,29}. Great advances in host-guest chemistry have been achieved in ultramicroporous MOFs with tailor-made properties for gas adsorption and separation, owing to the confinement effect from the strong host-guest interactions^{30–32}. Currently, the major interest in gas

¹Department of Chemical and Biomolecular Engineering, National University of Singapore, 117585 Singapore, Singapore. ²Department of Chemistry, The University of Manchester, Manchester M13 9PL, UK. ³School of Chemistry and Chemical Engineering, Guangxi University, Nanning 530004, China. ⁴College of Chemistry, Beijing Normal University, Beijing 100875, China. ⁵The European Synchrotron Radiation Facility, 71 Avenue des Martyrs, CS40220 Cedex 9, 38043 Grenoble, France. ⁶Diamond Light Source, Harwell Science Campus, Oxfordshire OX11 0DE, UK. ⁷College of Chemistry and Molecular Engineering, Beijing National Laboratory for Molecular Sciences, Peking University, Beijing 100871, China. ⁸These authors contributed equally: Zhaoqiang Zhang, Yinlin Chen.

✉ e-mail: sihai.yang@manchester.ac.uk; chezhao@nus.edu.sg

adsorption and separation using ultramicroporous MOFs is focused on enhancing recognition selectivity by tuning the host-guest interactions^{19,29,33–36}. This is pronounced for selective adsorption of acetylene (C_2H_2) from carbon dioxide (CO_2), as C_2H_2 is one of the most important industrial precursors, and the CO_2 contaminant would be coproduced during the production of C_2H_2 via partial combustion of natural gas^{34–36}. However, the understanding of the impact of guest-guest interactions or guest clusters on selectivity remains lacking due to the difficulties in the direct observation of such dynamic and weak interactions.

Herein, we report the modulation of geometries of guest-clusters as a function of temperature (Fig. 1) for the normal and inverse selectively and separation of CO_2 and C_2H_2 within the robust ultramicroporous M-CUK-1 (M = Co, Ni, and Mg) materials. The guest-guest interactions and binding domains within CUK-1 with different metal nodes have been observed by in-situ synchrotron X-ray diffractions and molecular simulations. The efficient packing of well-organized CO_2 clusters with T-shaped dimers gives rise to notably higher crystallographic occupancy and capacity of CO_2 (106 vs. $86\text{ cm}^3\text{ g}^{-1}$ of C_2H_2 in Co-CUK-1 at 298 K), while the stronger host-guest interactions between C_2H_2 and CUK-1 at room temperature lead CUK-1 to preferentially adsorb C_2H_2 over CO_2 (Fig. 1). Notably, a much larger increment of CO_2 capacities at low temperatures was observed compared with those of C_2H_2 , which is resulted from the highly efficient packing of CO_2 clusters with tetramers and the significantly stronger host-guest interactions between CO_2 and CUK-1. This finally leads to much higher CO_2 capacities ($170\text{ vs. }119\text{ cm}^3\text{ g}^{-1}$ of C_2H_2 at 233 K) and clear sorption inversion of CO_2 over C_2H_2 . Such an inverse CO_2/C_2H_2 adsorption behavior is more desirable for industrial production of C_2H_2 via a one-step CO_2 adsorption process but is rarely investigated^{18,29,37–40}. The temperature-dependent reversal of sorption behavior for CO_2 and C_2H_2 is demonstrated by gas sorption isotherms and dynamic breakthrough experiments at various temperatures. High-purity C_2H_2

(99.995%) can be directly obtained in a one-step process, and the low energy input for the regeneration suggests that CUK-1 is a promising adsorbent for C_2H_2 production via the temperature-swing adsorption (TSA) process.

Results

Materials and characterization

M-CUK-1 (M = Co, Ni, and Mg) were hydrothermally synthesized by reacting 2,4-pyridinedicarboxylic acid (2,4-H₂pdc) and M^{2+} -containing salts (M = Co, Ni, and Mg) with KOH in water at 210 °C for 24 h^{41–43}. The CUK-1 materials are isostructural. The edge- and vertex-sharing $M_3(\mu_3\text{-OH})_2$ chains serve as undulating pillars connecting the 2,4-pdc ligands in an orthogonal fashion, forming a ‘wine-rack’ topology with one-dimensional diamond-shaped and corrugated channels (Supplementary Fig. 1)^{41–43}. All three CUK-1 materials show excellent chemical and structural stability, and are entirely stable upon air exposure for two years (Supplementary Figs. 2–5). Desolvated CUK-1 exhibits an ultramicroporous structure, as evidenced by the negligible N_2 uptakes and typical type-I CO_2 isotherms at 77 K and 196 K, respectively (Supplementary Figs. 6–9). The calculated Brunauer–Emmett–Teller (BET) surface areas are 500–600 $\text{m}^2\text{ g}^{-1}$ based on the CO_2 isotherms. Upon desolvation, the exposed $\mu_3\text{-OH}$ groups reside orderly in the channels ($8.1 \times 10.6\text{ \AA}^2$, Supplementary Fig. 1), acting as potential binding sites to guest molecules through electrostatic interactions^{41–43}. This is highly desirable for the adsorption and separation of hydrocarbons.

Analysis of gas adsorption isotherms and selectivity

Adsorption isotherms of CO_2 and C_2H_2 on desolvated M-CUK-1 (M = Co, Ni, and Mg) at 298 K indicate the preferential adsorption of C_2H_2 at low pressure but higher saturation capacity of CO_2 upon increasing the pressure (Fig. 2a–c). This behavior results in the intersection of the two isotherms at moderate pressure. Another ultramicroporous compound, SIFSIX-3-Ni, exhibits similar isotherm crossing but with a stronger affinity to CO_2 at low pressures²⁹. After the intersection of CO_2 and C_2H_2 isotherms at 0.42 bar on Co-CUK-1, the CO_2 isotherm is above that of C_2H_2 , and CO_2 uptake at 1 bar can reach $106\text{ cm}^3\text{ g}^{-1}$, much higher than that of C_2H_2 ($86\text{ cm}^3\text{ g}^{-1}$, Fig. 2a). To the best of our knowledge, such an intersection between CO_2 and C_2H_2 isotherms is rarely observed on porous materials²⁹. Similarly, Ni- and Mg-CUK-1 show stronger sorption affinities to C_2H_2 in the low-pressure range, and the CO_2 and C_2H_2 isotherms also intersect but with relatively higher intersecting pressures of 0.6 and 0.95 bar on Ni- and Mg-CUK-1, respectively (Fig. 2b, c).

Considering that the inversed CO_2/C_2H_2 selectivity is more desirable for industrial C_2H_2 production, the respective guest loadings were measured at progressively lower temperatures to decrease the intersecting pressures. Upon reducing the temperature, there are significant enhancements for CO_2 uptakes but only a slight increase in C_2H_2 uptakes, finally leading to much higher CO_2 uptakes, even at very low pressures (Fig. 2a–c and Supplementary Figs. 7–9). Specifically, the CO_2 uptakes at 233 K are 170, 142, and $144\text{ cm}^3\text{ g}^{-1}$ on Co-, Ni-, and Mg-CUK-1 (ca. 4.15, 3.43, and 3.50 CO_2 molecules per cell, respectively), which notably exceed those of C_2H_2 (119, 97, and $89\text{ cm}^3\text{ g}^{-1}$, respectively; ca. 2.89, 2.29, and 2.32 C_2H_2 molecules per cell on Co-, Ni-, and Mg-CUK-1, respectively). The densities of adsorbed CO_2 molecules (based on the structural pore volume) in Co-, Ni-, and Mg-CUK-1 at 233 K were estimated to be 1.40, 1.27, and 1.25 g cm^{-3} , respectively. Notably, these densities are higher than that of liquid CO_2 (1.1 g cm^{-3}) but lower than that of dry ice ($1.55\text{ to }1.7\text{ g cm}^{-3}$)⁴⁴, indicating the highly efficient packing of CO_2 in the pores. However, the densities of adsorbed C_2H_2 molecules were recorded as only 0.56, 0.50, and 0.45 g cm^{-3} in Co-, Ni-, and Mg-CUK-1, respectively, lower than that of liquid C_2H_2 (0.69 g cm^{-3})⁴⁵. At 253 K and 233 K, there is a clear inversion in the adsorption selectivity from C_2H_2 to CO_2 on the CUK-1 materials. The uptake gap between CO_2 and C_2H_2 at 0.5 bar on

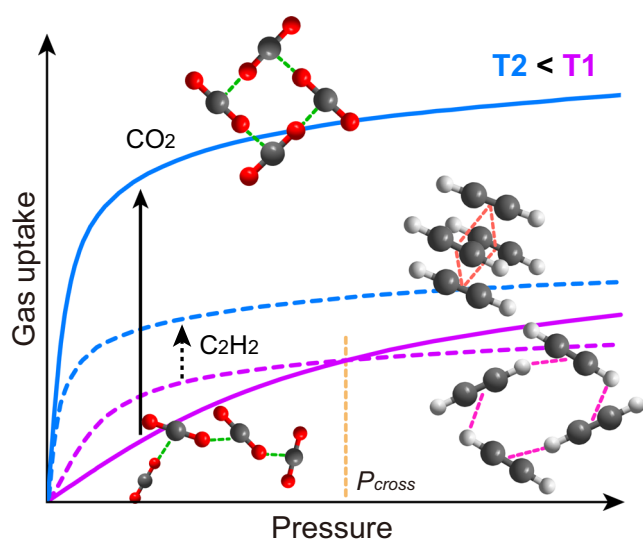


Fig. 1 | Illustration of the temperature-dependent packing geometries of guest clusters for the normal and inverse adsorption behavior. At a high temperature (T1, purple), the strong host-guest and guest-guest interactions result in preferential adsorption of C_2H_2 , but the efficient packing of molecular chains formed by CO_2 molecules through strong guest-guest interactions leads to the higher uptake at the high-pressure range ($>P_{\text{cross}}$). After decreasing the temperature to T2 (blue), the CO_2 clusters with T-shaped dimers exhibit higher occupancy of the pore channels than that of C_2H_2 clusters packed together via $\pi\cdots\pi$ interactions, coupled with the strong host-guest interactions, leading to the inverse CO_2 preferential sorption.

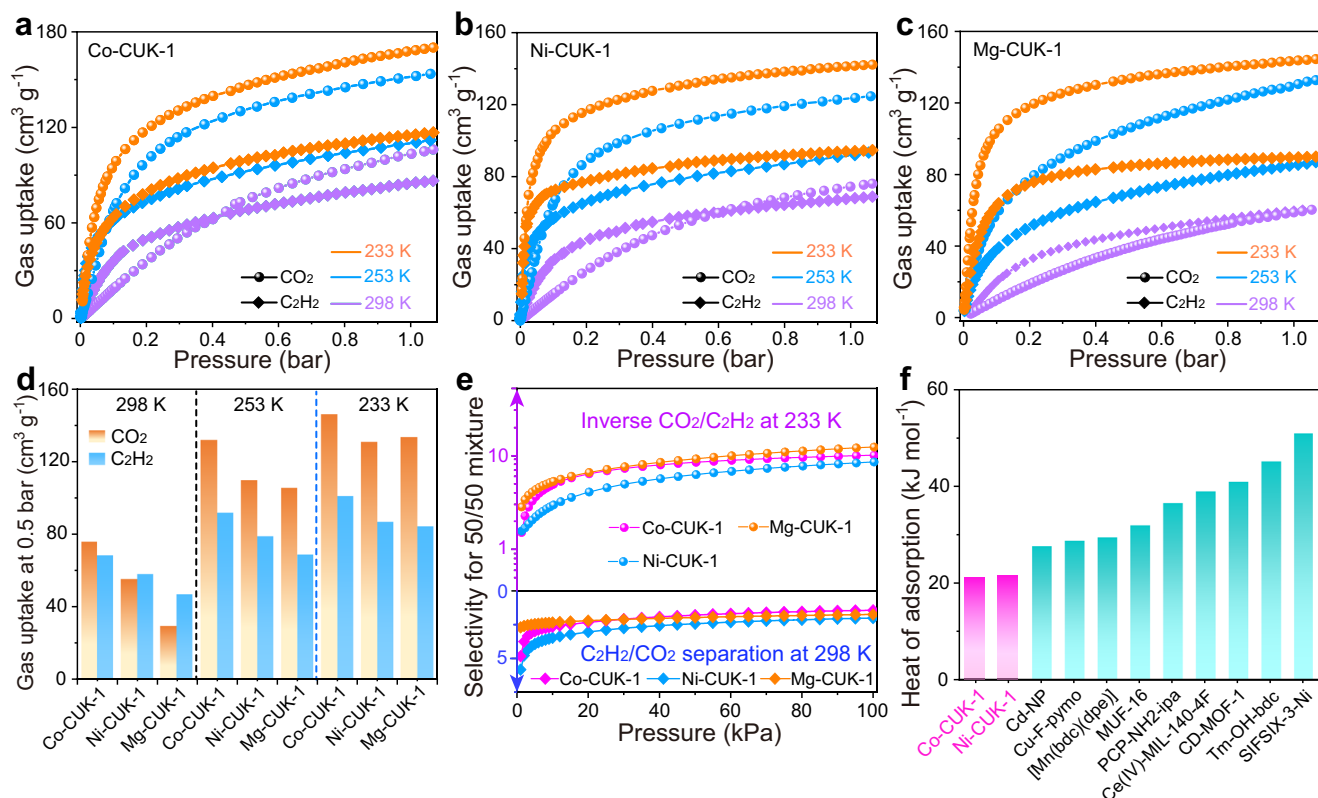


Fig. 2 | CO₂ and C₂H₂ adsorption and separation performance on CUK-1 materials. The CO₂ and C₂H₂ adsorption isotherms on desolvated Co-CUK-1 (a), Ni-CUK-1 (b), and Mg-CUK-1 (c) at 298 (purple), 253 (blue), and 233 K (orange). d The comparison of CO₂ and C₂H₂ uptakes at 0.5 bar on CUK-1 materials at different

temperatures. e The inverse CO₂/C₂H₂ (1/1) (top) and normal C₂H₂/CO₂ (1/1) (bottom) selectivities at 233 and 298 K, respectively, on CUK-1 materials. f Comparison of the zero-coverage heat of adsorption of CUK-1 materials for CO₂ with those of other materials for inverse CO₂/C₂H₂ separation.

Co-CUK-1 can reach 40 and 45 cm³ g⁻¹ at 253 and 233 K (Fig. 2d), respectively.

State-of-the-art C₂H₂/CO₂ separation is mainly realized by cryogenic distillation and solvent absorption with high energy penalty. The adsorptive separation using CO₂-selective other than C₂H₂-selective materials is preferable in the industry for producing pure C₂H₂ via one-step sorption procedures. To see whether such a temperature-induced adsorption inversion behavior can be used for inverse CO₂/C₂H₂ separation, we evaluated CUK-1 materials for separating the equimolar mixture of CO₂/C₂H₂ by analyzing the single-component isotherms via ideal adsorbed solution theory (IAST). At 298 K, CUK-1 only shows a moderate C₂H₂/CO₂ selectivity of ca. 2. However, at 233 K, CUK-1 exhibits the inverted CO₂/C₂H₂ selectivity of 9.5, 8.4, and 12.1 for Co-, Ni-, and Mg-CUK-1, respectively (Fig. 2e). The inverted selectivities are comparable with those of the state-of-the-art materials for inverse CO₂/C₂H₂ separation, such as [Mn(bdc)(bpe)] (9)⁴⁶, Ce(IV)-MIL-140-4F (9.6)³⁷, PCP-NH₂-ipa (6.4)³⁵, and SIFSIX-3-Ni (7.5)²⁹, but lower than the benchmark material Cu-F-pymo (> 10⁵)³⁸. Furthermore, the isosteric heats of adsorption (ΔH_{ads}) of CO₂ on Co- and Ni-CUK-1 were calculated to be 20.8 and 21.7 kJ mol⁻¹, respectively (Supplementary Fig. 10), much lower than that of other materials (Fig. 2f), such as PCP-NH₂-ipa (26.8 kJ mol⁻¹)³⁵, [Mn(bdc)(bpe)] (29.5 kJ mol⁻¹)⁴⁶, MUF-16 (32 kJ mol⁻¹)³⁹, and Tm₂(OH-bdc) (45 kJ mol⁻¹)⁴⁰.

Guest configurations determined by in-situ synchrotron X-ray powder diffraction

In-situ synchrotron X-ray powder diffraction data on CO₂- and C₂H₂-loaded CUK-1 materials were collected as a function of temperature (Supplementary Figs. 11–12). Full refinements of the data indicate two binding sites in the asymmetric unit: site I is close to the μ_3 -OH group,

and site II locates near the pore surface (Figs. 3–4 and Supplementary Figs. 13–18). At 298 K, the total crystallographic occupancy of C₂H₂ molecules (2.05 per cell) in Co-CUK-1 is in excellent agreement with that obtained from the isotherm (2.07 C₂H₂ per cell). C₂H₂ molecules at site I locate almost perpendicular to μ_3 -OH groups, forming O-H $\cdots\pi_{C_2H_2}$ H-bonds (2.92 Å, dotted green lines), supplemented by additional interactions via C-H_{C₂H₂} \cdots O_{ligand} H-bonding (dotted green lines, 2.67–2.71 Å, Fig. 3a and Supplementary Fig. 13a). C₂H₂ molecules at site II sit close to the aromatic rings on the pore surface and form weak interactions with the framework through multiple C-H_{C₂H₂} \cdots O_{ligand} H-bonding (3.37–3.82 Å) and $\pi_{C_2H_2}\cdots H_{ligand}$ (3.44–3.67 Å) interactions. Moreover, at high loading, the neighboring C₂H₂ molecules synergistically interact with each other through multiple H_{C₂H₂} $\cdots\pi_{C_2H_2}$ interactions (dotted pink lines, 2.33–2.95 Å), forming the tetramer-clusters of C₂H₂ (Fig. 3b).

In contrast, CO₂ molecules show different geometries of packing (Fig. 3c and Supplementary Fig. 14a). CO₂ molecules at site I exhibit an end-on interaction to μ_3 -OH group via hydrogen bonds (dotted lime lines, 2.42 Å of O-H \cdots O_{CO₂}), but no interactions between CO₂ and the ligand of CUK-1 were observed. CO₂ molecules at site II interact with the pore surface via weak O-H_{ligand} interactions (3.88–3.91 Å, Supplementary Fig. 14a). Thus, adsorbed CO₂ molecules at both sites show much weaker interactions compared with C₂H₂, entirely consistent with the adsorption results at room temperature. However, at high loading, two one-dimensional chains of CO₂ (dotted azure lines) running along the channel were formed via strong guest-guest interactions (2.93 and 2.74 Å, Fig. 3d). These chains are stabilized by multiple weak intermolecular dipole interactions between monomer-to-dimer and dimer-to-dimer of CO₂. Furthermore, two chains interact with each other via multiple synergistic host-host interactions (dotted green

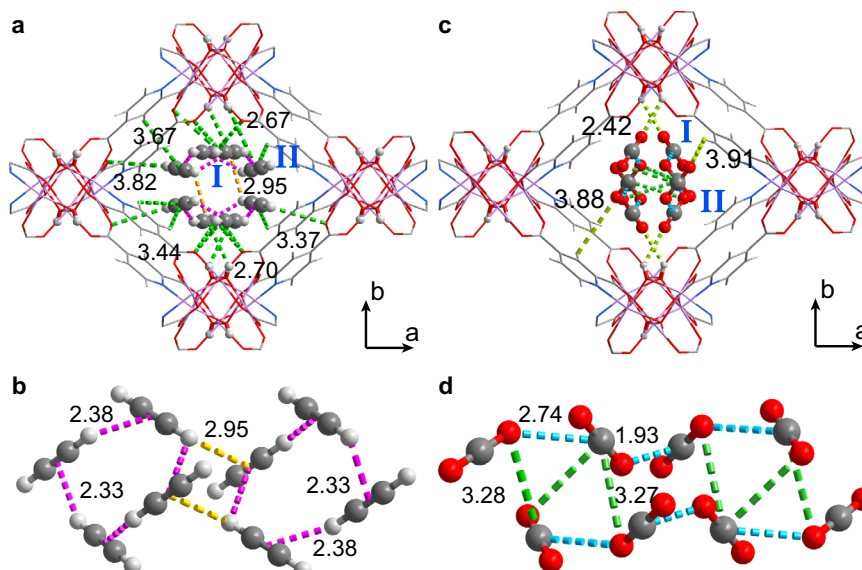


Fig. 3 | Configurations of adsorbed C₂H₂ and CO₂ molecules within Co-CUK-1 from refinements of in-situ synchrotron X-ray powder diffraction data at 298 K. Views of host-guest interactions of C₂H₂ (a) and CO₂ (c) in Co-CUK-1. Packing

geometries of C₂H₂ (b) and CO₂ (d) clusters. Color code: C, gray; H, gray-25%; O, red; N, blue; Co, pink.

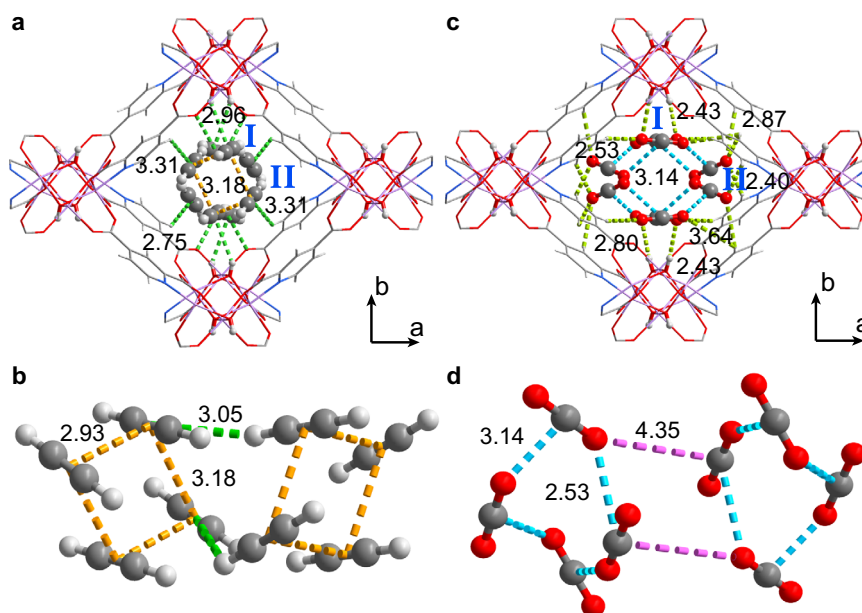


Fig. 4 | Configurations of adsorbed C₂H₂ and CO₂ molecules within Co-CUK-1 from refinements of in-situ synchrotron X-ray powder diffractions at 233 K. Views of host-guest interactions between C₂H₂ (a) and CO₂ (c) in Co-CUK-1. Packing

geometries of C₂H₂ (b) and CO₂ (d) clusters. Color code: C, gray; H, gray-25%; O, red; N, blue; Co, pink.

lines, 3.27–3.28 Å). Notably, the neighboring CO₂ molecules exhibit a head-to-center (C=O...C) geometry (Supplementary Fig. 14a), thus leading to the efficient packing of CO₂ in the pore channels. Similar binding sites of CO₂ in Ni-CUK-1 were also observed (Supplementary Fig. 18). Compared with C₂H₂ clusters, the efficient packing of CO₂ molecules near the center of pore channels via strong guest-guest interactions but with less host-guest interactions is the main reason for the high adsorption of CO₂ in CUK-1 at high pressures.

At 233 K, remarkable changes in the packing geometry of CO₂ and C₂H₂ were observed (Fig. 4), and the crystallographic occupancy of C₂H₂ molecules increased to 2.77 per cell. Meanwhile, the CO₂ occupancy increased to 3.47 per cell (vs. 2.07 at 298 K), indicating the high

capacity of Co-CUK-1 for CO₂ at 233 K compared with that for C₂H₂. This is entirely consistent with the isotherms. C₂H₂ molecules at site I interact with bridging μ_3 -OH groups via $\pi_{\text{C}_2\text{H}_2} \cdots \text{H}-\text{O}$ H-bond (2.96 Å) that is supplemented by weak C-H...O_{ligand} H-bonding (dotted green lines, 2.75 Å, Fig. 4a and Supplementary Fig. 13b). CO₂ molecules at site I are stabilized by C-O_{CO2}...H _{μ_3 -OH} H-bonding (2.43 Å) and C-O_{CO2}...H_{ligand} interactions (2.80 and 3.64 Å, Fig. 4c and Supplementary Fig. 14b). C₂H₂ molecules at site II reside near the center of pore channels with fewer host-guest interactions ($\pi \cdots \text{H}_{\text{ligand}}$ 3.31 Å), similar to that of CO₂ in the channels at 298 K. However, CO₂ molecules are located in the corner of the pore channels and stabilized by multiple weak host-guest interactions (C-O_{CO2}...H_{ligand}, 2.40–2.87 Å), thus

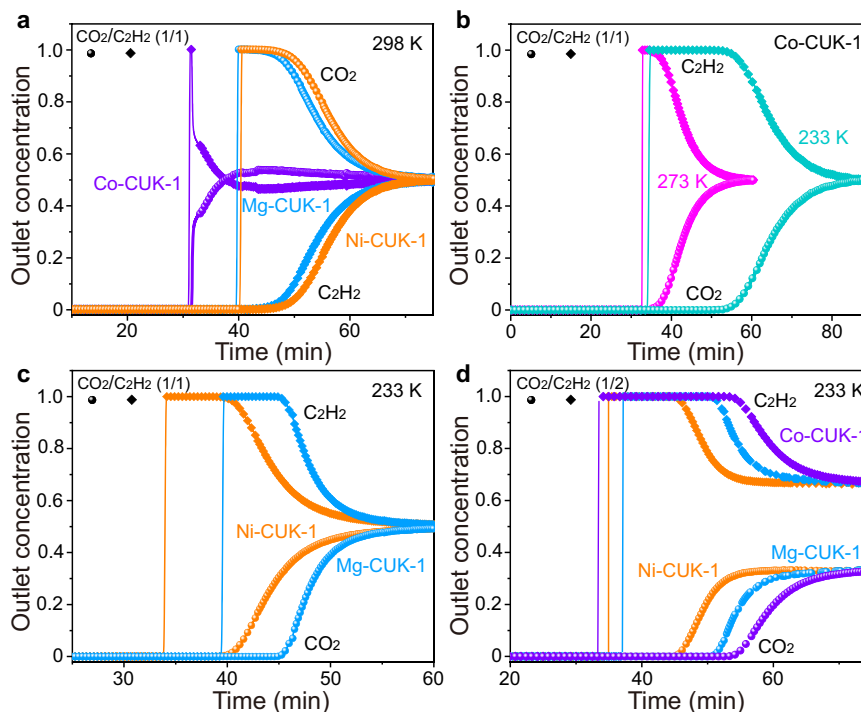


Fig. 5 | Breakthrough curves of CUK-1 materials for CO₂/C₂H₂ mixtures.

a Breakthrough curves of CO₂/C₂H₂ (1/1) mixture on CUK-1 materials at 298 K with a flow rate of 2.0 mL min⁻¹. **b** Breakthrough curves of CO₂/C₂H₂ (1/1) mixture on Co-CUK-1 at 273 and 233 K with flow rates of 2.0 and 3.0 mL min⁻¹, respectively.

c Breakthrough curves of CO₂/C₂H₂ (1/1) mixture on Ni-CUK-1 and Mg-CUK-1 at 233 K with a flow rate of 3.0 mL min⁻¹. **d** Breakthrough curves of CO₂/C₂H₂ (1/2) mixture on CUK-1 materials at 233 K with a flow rate of 3.0 mL min⁻¹.

leading to the strong binding affinities of host framework for CO₂. Meanwhile, in Co-CUK-1, C₂H₂ clusters are formed with C₂H₂ molecules via $\pi_{C_2H_2} \cdots \pi_{C_2H_2}$ interactions (dotted orange lines, 2.95 and 3.18 Å, Fig. 4b). The neighboring clusters synergistically interact with each other via weak C-H \cdots π H-bonding (3.05 and 3.17 Å), leading to the efficient packing of C₂H₂ molecules. By contrast, the isolated CO₂ clusters are formed with four CO₂ molecules by closely interacting with each other (distances of 2.53 and 3.14 Å) with the head-to-center configurations, forming the quasi-T-shaped geometry (C=O \cdots C, dotted azure lines, Fig. 4d). This is similar to that in dry ice, indicating the highly efficient packing of CO₂ molecules (thus packing densities) in Co-CUK-1. Similar CO₂ clusters with quasi-T-shaped dimers were also observed in Ni-CUK-1 at 233 K (Supplementary Fig. 16d). Thus, the notably stronger guest-guest interactions between adsorbed CO₂ molecules at low temperature promote the unusually selective adsorption of CO₂ over C₂H₂ at 233 K. Importantly, to the best of our knowledge, such guest-guest packing geometries and host-guest interactions at different temperatures have not been observed in porous materials yet.

To quantitatively compare the binding affinities of CUK-1 to CO₂ and C₂H₂ at different temperatures, the static binding energies (ΔE) were further estimated by first-principles density functional theory (DFT) calculations (Supplementary Tables 2 and 3). The results show that after decreasing the temperature from 298 to 233 K, there are significant increases of ΔE at site I for CO₂. Especially, ΔE for CO₂ at site I on Co-CUK-1 is 43.5 kJ mol⁻¹, much higher than that for C₂H₂ (33.3 kJ mol⁻¹), directly validating the preferential adsorption of CO₂ over C₂H₂. There is a subtle difference in host-guest interactions when varying the metal nodes in CUK-1 (Supplementary Tables 2 and 3), and this has little influence on the formation of guest clusters and the tunable CO₂ and C₂H₂ sorption behavior. Thus, the guest-guest interactions and/or the arrangement of guest clusters play the dominant role in the inverse CO₂ sorption of CUK-1 materials.

Dynamic breakthrough tests

Dynamic breakthrough experiments on CUK-1 materials using mixtures of CO₂/C₂H₂ were conducted (Fig. 5). For the equimolar CO₂/C₂H₂ mixture at 298 K, Ni- and Mg-CUK-1 show typical C₂H₂-preferential sorption over CO₂ with a clear separation of C₂H₂ and CO₂, but Co-CUK-1 shows very poor separation (Fig. 5a and Supplementary Fig. 19). These are consistent with the isotherm results at 298 K. At 273 K, a clear inverted CO₂/C₂H₂ separation was observed on Co-CUK-1 (Fig. 5b and Supplementary Fig. 20), and there is an obvious deterioration in C₂H₂/CO₂ separation performance on Ni- and Mg-CUK-1 (Supplementary Fig. 21). At 233 K, an evident inverted CO₂/C₂H₂ separation was observed on CUK-1 materials, and all materials exhibit highly selective adsorption of CO₂ over C₂H₂ (Fig. 5b, c). The dynamic CO₂ uptake capacities at 233 K were calculated to be 140, 110, and 122 cm³ g⁻¹ on Co-, Ni-, and Mg-CUK-1, respectively, much higher than those of C₂H₂ (62, 67, and 78 cm³ g⁻¹, respectively). To mimic the industrial processes for C₂H₂ production, we further studied a gas mixture of CO₂/C₂H₂ (1/2). A complete inverted CO₂/C₂H₂ separation was realized with CO₂ retained in the fixed bed for a longer duration (Fig. 5d). Significantly, the productivity of pure C₂H₂ (99.995%) can reach 62 and 41.7 L kg⁻¹ on Co-CUK-1 and Mg-CUK-1, respectively, much higher than that on MUF-16 (27 L kg⁻¹)³⁹ and Cu-F-pymo (3.7 L kg⁻¹)³⁸. It is worth noting that these materials show excellent cycling separation performance and can be easily regenerated by purging helium (He) at 298 K (Supplementary Figs. 22–23). The notably high CO₂ uptake and facile regeneration of CUK-1 are particularly desirable for practical applications to reduce the energy footprint compared with state-of-the-art cryogenic distillations.

Discussion

In summary, we report the direct observation of packing geometry rearrangement of gas clusters as a function of temperature to control the adsorption selectivity of CO₂ and C₂H₂ on ultramicroporous MOFs.

The strong host-guest interactions of CUK-1 for C₂H₂ at ambient conditions led to the preferential adsorption of C₂H₂. However, the efficient packing of CO₂ molecules via strong guest-guest interactions forms CO₂ clusters, leading to higher CO₂ capacity. Impressively, after decreasing temperature, the host-guest interactions between CO₂ and host framework became stronger than that for C₂H₂. Furthermore, the highly ordered arrangement of CO₂ clusters with the T-shaped dimers endows CUK-1 with remarkably higher capacities for CO₂ over those for C₂H₂. Such host-guest interactions, guest-guest interactions, and gas cluster formation were elucidated by in-situ synchrotron X-ray powder diffraction and molecular simulations. This idiosyncratic inversion of the adsorption behavior of C₂H₂ and CO₂ was verified by dynamic breakthrough experiments with high-purity C₂H₂ (99.995%) obtained in a one-step process. Furthermore, the fixed-bed packed with CUK-1 can be easily regenerated at room temperature by purging an inert gas, indicating that the TSA process using CUK-1 materials is highly efficient for C₂H₂ production.

Methods

Gas adsorption and separation experiments

CO₂ and C₂H₂ sorption isotherms were collected at different temperatures on a Micromeritics ASAP 2020 instrument equipped with commercial software for data calculation and analysis. The test temperatures were controlled by soaking the sample cell in a circulating water bath (298 K), ice/methanol mixture (233–273 K), dry ice/acetone mixtures (196 K), or liquid N₂ (77 K). Before measurement, the sample (80–100 mg) was degassed at 423 K for 24 h. The breakthrough experiments were performed in a stainless-steel fixed bed (4.6 mm inner diameter × 50 mm length) packed with ~0.6 g of CUK-1 powder. Before the breakthrough experiment, the fixed bed was heated at 423 K under a flow of He for complete activation. The fixed bed was then cooled to room temperature and immersed in a water/methanol bath with different temperatures. Then, the gas mixtures (C₂H₂/CO₂) were introduced, and the outlet gas was monitored by mass spectrometry (Hidden QGA quantitative gas analysis system).

In-situ synchrotron powder X-ray diffraction and structure determination

Fresh samples of Co-CUK-1 or Ni-CUK-1 were pre-activated under a dynamic vacuum at 200 °C, then loaded into a 0.7 mm borosilicate capillary under an inert atmosphere. Then the capillary was further activated by heating to 100 °C under a dynamic vacuum for 2 h before cooling down to room temperature. For samples measured under 233 K, synchrotron X-ray powder diffraction was carried out on the ID22 high-resolution powder diffraction beamline at the European Synchrotron Radiation Facility (ESRF). C₂H₂ or CO₂ was introduced into the capillary, and diffraction data were collected after one-hour stabilization. Data were measured between 0 and 35° with a 13-channel multi-analyzer stage under the wavelength of 0.354267(4) Å. Data were binned using a step size of 0.002°. For samples measured under 298 K, high-resolution powder X-ray diffraction patterns were collected on the powder diffractometer (λ = 0.825829(1) Å) at room temperature on beamline I11 (Diamond Light Source, UK). C₂H₂ or CO₂ was dosed offline and then sealed for measurement. Data were collected between 0 and 150° using a step size of 0.001° with five multi-analyzing crystal (MAC) detectors without further re-binned.

Pawley and Rietveld refinements of the structure were carried out using the TOPAS software package (roughly between 18–0.90 Å in d-spacing). Due to the high flexibility of the framework, index with constraints was used to get the information on cell parameters and space groups. Stepwise fitting was applied to describe the diffraction peaks and their anisotropic broadening. Approximate positions of the guest molecule under a rigid body model were found using the

simulated annealing approach before further refinement was used to find the optimal orientation of the guest molecules. The final refined structural parameters include cell parameters, the fractional coordinates (x, y, z) and isotropic displacement factors for all atoms except hydrogen, and the site occupancy factors (SOF) for guest molecules. The accuracy of the final model was verified by the convergence of the weighted profile factor (R_{wp}), the chemical sense of the model, and the good correlation between the observed and calculated diffraction patterns.

Data availability

Crystallographic data for the structures reported in this article have been deposited at the Cambridge Crystallographic Data Centre under deposition numbers CCDC 2214437, 2214440–2214446. These data can be obtained free of charge via <https://www.ccdc.cam.ac.uk/structures/>. All the other relevant data, additional graphics, and calculations that support the findings of this study are available within the article and its Supplementary Information, or from the corresponding authors upon request.

References

1. Beer, P., Barendt, T. A., Lim, J. Y. C. *Supramolecular Chemistry: Fundamentals and Applications*. (Oxford university press, 2022).
2. Lehn, J. M. Supramolecular chemistry: Where from? Where to? *Chem. Soc. Rev.* **46**, 2378–2379 (2017).
3. Kolesnichenko, I. V. & Anslyn, E. V. Practical applications of supramolecular chemistry. *Chem. Soc. Rev.* **46**, 2385–2390 (2017).
4. Yang, S. et al. Supramolecular binding and separation of hydrocarbons within a functionalized porous metal-organic framework. *Nat. Chem.* **7**, 121–129 (2014).
5. Smith, G. L. et al. Reversible coordinative binding and separation of sulfur dioxide in a robust metal-organic framework with open copper sites. *Nat. Mater.* **18**, 1358–1365 (2019).
6. Shimomura, S. et al. Selective sorption of oxygen and nitric oxide by an electron-donating flexible porous coordination polymer. *Nat. Chem.* **2**, 633–637 (2010).
7. Yoon, J. W. et al. Selective nitrogen capture by porous hybrid materials containing accessible transition metal ion sites. *Nat. Mater.* **16**, 526–531 (2017).
8. Jaramillo, D. E. et al. Selective nitrogen adsorption via backbonding in a metal-organic framework with exposed vanadium sites. *Nat. Mater.* **19**, 517–521 (2020).
9. Schneemann, A. et al. Flexible metal-organic frameworks. *Chem. Soc. Rev.* **43**, 6062–6096 (2014).
10. Wang, S. et al. Toward a rational design of titanium metal-organic frameworks. *Matter* **2**, 440–450 (2020).
11. He, T. et al. Trace removal of benzene vapour using double-walled metal-dipyrazolate frameworks. *Nat. Mater.* **21**, 689–695 (2022).
12. Adil, K. et al. Gas/vapour separation using ultra-microporous metal-organic frameworks: Insights into the structure/separation relationship. *Chem. Soc. Rev.* **46**, 3402–3430 (2017).
13. Ebadi Amooghin, A., Sanaeepur, H., Luque, R., Garcia, H. & Chen, B. Fluorinated metal-organic frameworks for gas separation. *Chem. Soc. Rev.* **51**, 7427–7508 (2022).
14. Ji, Z., Wang, H., Canossa, S., Wuttke, S. & Yaghi, O. M. Pore chemistry of metal-organic frameworks. *Adv. Funct. Mater.* **30**, 2000238 (2020).
15. Yang, Q., Xu, Q. & Jiang, H. L. Metal-organic frameworks meet metal nanoparticles: synergistic effect for enhanced catalysis. *Chem. Soc. Rev.* **46**, 4774–4808 (2017).
16. Bloch, E. D. et al. Hydrocarbon separations in a metal-organic framework with open iron (II) coordination sites. *Science* **335**, 1606–1610 (2012).

- Evans, J. D., Bon, V., Senkovska, I., Lee, H. C. & Kaskel, S. Four-dimensional metal-organic frameworks. *Nat. Commun.* **11**, 2690 (2020).
- Ma, Y. et al. A convenient strategy for designing a soft nanospace: an atomic exchange in a ligand with isostructural frameworks. *J. Am. Chem. Soc.* **137**, 15825–15832 (2015).
- Cui, X. et al. Pore chemistry and size control in hybrid porous materials for acetylene capture from ethylene. *Science* **353**, 141–144 (2016).
- Li, J. et al. Capture of nitrogen dioxide and conversion to nitric acid in a porous metal-organic framework. *Nat. Chem.* **11**, 1085–1090 (2019).
- Hu, J. & Liu, S. Engineering responsive polymer building blocks with host-guest molecular recognition for functional applications. *Acc. Chem. Res.* **47**, 2084–2095 (2014).
- Islamoglu, T. et al. Metal-organic frameworks against toxic chemicals. *Chem. Rev.* **120**, 8130–8160 (2020).
- Zeng, H. et al. Orthogonal-array dynamic molecular sieving of propylene/propane mixtures. *Nature* **595**, 542–548 (2021).
- O’Keeffe, M. & Yaghi, O. M. Deconstructing the crystal structures of metal-organic frameworks and related materials into their underlying nets. *Chem. Rev.* **112**, 675–702 (2012).
- Liao, P. Q., Huang, N. Y., Zhang, W. X., Zhang, J. P. & Chen, X. M. Controlling guest conformation for efficient purification of butadiene. *Science* **356**, 1193–1196 (2017).
- Wang, S. et al. A robust large-pore zirconium carboxylate metal-organic framework for energy-efficient water-sorption-driven refrigeration. *Nat. Energy* **3**, 985–993 (2018).
- Matsuda, R. et al. Highly controlled acetylene accommodation in a metal-organic microporous material. *Nature* **436**, 238–241 (2005).
- Schoedel, A., Li, M., Li, D., O’Keeffe, M. & Yaghi, O. M. Structures of metal-organic frameworks with rod secondary building units. *Chem. Rev.* **116**, 12466–12535 (2016).
- Chen, K. J. et al. Benchmark C₂H₂/CO₂ and CO₂/C₂H₂ separation by two closely related hybrid ultramicroporous materials. *Chem.* **1**, 753–765 (2016).
- Han, X. & Yang, S. Molecular mechanisms behind acetylene adsorption and selectivity in functional porous materials. *Angew. Chem. Int. Ed.* **62**, e202218274 (2023).
- Zhao, X., Wang, Y., Li, D. S., Bu, X. & Feng, P. Metal-organic frameworks for separation. *Adv. Mater.* **30**, e1705189 (2018).
- Li, J. R., Sculley, J. & Zhou, H. C. Metal-organic frameworks for separations. *Chem. Rev.* **112**, 869–932 (2012).
- Cui, W. G., Hu, T. L. & Bu, X. H. Metal-organic framework materials for the separation and purification of light hydrocarbons. *Adv. Mater.* **32**, e1806445 (2020).
- Zhang, Z. et al. Efficient trapping of trace acetylene from ethylene in an ultramicroporous metal-organic framework: Synergistic effect of high-density open metal and electronegative sites. *Angew. Chem. Int. Ed.* **59**, 18927–18932 (2020).
- Gu, Y. et al. Host-guest interaction modulation in porous coordination polymers for inverse selective CO₂/C₂H₂ separation. *Angew. Chem. Int. Ed.* **60**, 11688–11694 (2021).
- Niu, Z. et al. A MOF-based ultra-strong acetylene nano-trap for highly efficient C₂H₂/CO₂ separation. *Angew. Chem. Int. Ed.* **60**, 5283–5288 (2021).
- Zhang, Z. et al. Optimal pore chemistry in an ultramicroporous metal-organic framework for benchmark inverse CO₂/C₂H₂ separation. *Angew. Chem. Int. Ed.* **60**, 17198–17204 (2021).
- Shi, Y. et al. Highly selective adsorption of carbon dioxide over acetylene in an ultramicroporous metal-organic framework. *Adv. Mater.* **33**, 2105880 (2021).
- Qazvini, O. T., Babarao, R. & Telfer, S. G. Selective capture of carbon dioxide from hydrocarbons using a metal-organic framework. *Nat. Commun.* **12**, 197 (2021).
- Ma, D. et al. Inverse and highly selective separation of CO₂/C₂H₂ on a thulium-organic framework. *J. Mater. Chem. A* **8**, 11933–11937 (2020).
- Yoon, J. W. et al. Gas-sorption selectivity of CUK-1: a porous coordination solid made of cobalt(II) and pyridine-2,4-dicarboxylic acid. *Adv. Mater.* **19**, 1830–1834 (2007).
- Humphrey, S. M., Chang, J. S., Jhung, S. H., Yoon, J. W. & Wood, P. T. Porous cobalt (II)-organic frameworks with corrugated walls: Structurally robust gas-sorption materials. *Angew. Chem. Int. Ed.* **119**, 276–279 (2007).
- Saccoccia, B. et al. Separation of p-divinylbenzene by selective room-temperature adsorption inside Mg-CUK-1 prepared by aqueous microwave synthesis. *Angew. Chem. Int. Ed.* **54**, 5394–5398 (2015).
- Mangan, T. P., Salzmann, C. G., Plane, J. M. C. & Murray, B. J. CO₂ ice structure and density under Martian atmospheric conditions. *Icarus* **294**, 201–208 (2017).
- McIntosh, D. The physical properties of liquid and solid acetylene. *J. Phys. Chem.* **11**, 306–317 (1907).
- Foo, M. L. et al. An adsorbate discriminatory gate effect in a flexible porous coordination polymer for selective adsorption of CO₂ over C₂H₂. *J. Am. Chem. Soc.* **138**, 3022–3030 (2016).

Acknowledgements

This work was supported by the Ministry of Education Singapore (MOE2019-T2-1-093, MOE-T2EP10122-0002; D.Z.), the Energy Market Authority of Singapore (EMA-EP009-SEGC-020; D.Z.), the Agency for Science, Technology and Research (U2102d2004, U2102d2012; D.Z.), the National Research Foundation (NRF-CRP26-2021RS-0002; D.Z.), EPSRC (EP/V056409/1; S.Y.), and the University of Manchester. We are grateful to Diamond Light Source and European Synchrotron Radiation Facility (ESRF) for access to Beamlines I11 and ID22, respectively. X.H. is supported by a Dame Kathleen Ollerenshaw Fellowship.

Author contributions

D.Z. and S.Y. formulated and supervised the project. Z.Z. synthesized and characterized the materials, measured the adsorption isotherms and the breakthrough curves, and wrote the manuscript. Y.C., X.H., C.D., S.J.D., and S.Y. collected and analyzed the in-situ synchrotron X-ray diffraction data. K.C. and C.K. helped collect the dynamic breakthrough data. S.P., H.L., J.R., and X.S. contributed to the data analysis and discussion. All authors contributed to the manuscript revision.

Competing interests

The authors declare no competing interests.

Additional information

Supplementary information The online version contains supplementary material available at <https://doi.org/10.1038/s41467-023-39319-2>.

Correspondence and requests for materials should be addressed to Sihai Yang or Dan Zhao.

Peer review information *Nature Communications* thanks Nyasha Makeve, and the other, anonymous, reviewer(s) for their contribution to the peer review of this work. A peer review file is available.

Reprints and permissions information is available at <http://www.nature.com/reprints>

Publisher’s note Springer Nature remains neutral with regard to jurisdictional claims in published maps and institutional affiliations.

Open Access This article is licensed under a Creative Commons Attribution 4.0 International License, which permits use, sharing, adaptation, distribution and reproduction in any medium or format, as long as you give appropriate credit to the original author(s) and the source, provide a link to the Creative Commons license, and indicate if changes were made. The images or other third party material in this article are included in the article's Creative Commons license, unless indicated otherwise in a credit line to the material. If material is not included in the article's Creative Commons license and your intended use is not permitted by statutory regulation or exceeds the permitted use, you will need to obtain permission directly from the copyright holder. To view a copy of this license, visit <http://creativecommons.org/licenses/by/4.0/>.

© The Author(s) 2023